Space-Filling X-Ray Source Trajectories for Efficient Scanning in Large-Angle Cone-Beam Computed Tomography

Andrew M. Kingston ⬤, Glenn R. Myers, Shane J. Latham, Benoit Recur ⬤, Heyang Li, and Adrian P. Sheppard ⬤

Abstract—**We present a new family of X-ray source scanning trajectories for large-angle cone-beam computed tomography. Traditional scanning trajectories are described by continuous paths through space, e.g., circles, saddles, or helices, with a large degree of redundant information in adjacent *projection* images. Here, we consider discrete trajectories as a set of points that uniformly sample the entire space of possible source positions, i.e., a *space-filling* trajectory (SFT). We numerically demonstrate the advantageous properties of the SFT when compared with circular and helical trajectories as follows: first, the most isotropic sampling of the data, second, optimal level of mutually independent data, and third, an improved condition number of the tomographic inverse problem. The practical implications of these properties in tomography are also illustrated by simulation. We show that the SFT provides greater data acquisition efficiency, and reduced reconstruction artifacts when compared with helical trajectory. It also possesses an effective preconditioner for fast iterative tomographic reconstruction.**

Index Terms—**Tomography, computed Tomography, X-rays, microscopy, trajectory optimization, sampling methods, robustness.**

I. INTRODUCTION

X-RAY cone-beam computed tomography (CBCT) is a non-destructive tool that can provide high-resolution, high-quality, three-dimensional (3D) structural information of

A. M. Kingston, G. R. Myers, S. J. Latham, and A. P. Sheppard are with the Department of Applied Mathematics, Research School of Physics and Engineering, The Australian National University, Canberra, ACT 2601, Australia, and also with CTLab: National Laboratory for Micro Computed-Tomography, Advanced Imaging Precinct, The Australian National University, Canberra, ACT 2601, Australia (e-mail: Andrew.Kingston@anu.edu.au; glenn.myers@anu.edu.au; shane.latham@anu.edu.au; adrian.sheppard@anu.edu.au).

B. Recur is with the University of Bordeaux, Inserm U1029 LAMC (Angiogenesis and Cancer Micro-environment Lab), Allée Geoffroy Stain-Hilaire, Bât B2, F33600 Pessac, France, and also with the Department of Applied Mathematics, Research School of Physics and Engineering, The Australian National University, Canberra, ACT 2601, Australia (e-mail: benoit.recur@gmail.com).

H. Li is with the Real Options and Financial Risk Team, Optimisation and Risk Analytics Group, Data61 Commonwealth Scientific and Industrial Research Organisation, Clayton, Vic 3168, Australia, and also with the Department of Applied Mathematics, Research School of Physics and Engineering, The Australian National University, Canberra, ACT 2601, Australia (e-mail: thomas.li@csiro.au).

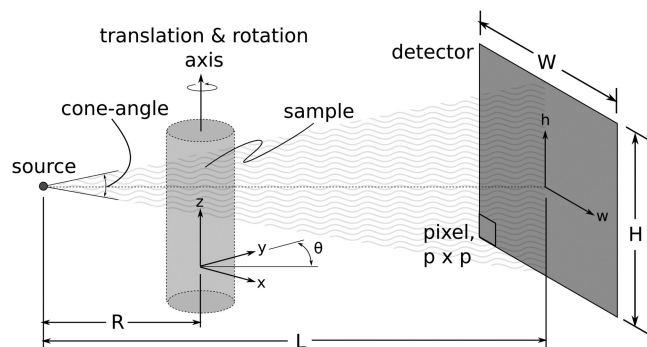Digital Object Identifier 10.1109/TCI.2018.2841202

Fig. 1. Ideal geometry of a fine-focus cone-beam CT system for 3D microscopy comprised of an X-ray source, sample manipulators (rotation stage and possibly a translation stage) and an X-ray detector.

specimens. In many cases, particularly with dual-energy scanning (e.g., [1]), it can also provide compositional information. Analysis of these 3D tomographic images is yielding new insights into a broad range of subject areas including palaeontology [2], geology [3], and materials science [4].

The system components and geometry of a CBCT microscope are presented in Fig. 1. A fine-focus geometry is depicted that provides optics-free (or lensless) geometrical magnification due to the spherical wave propagation of X-rays from a micro-focus X-ray source. The sample is not directly imaged in 3D from this instrument, rather, the 3D information of the sample (or specimen) is projected onto a 2D detector and recorded as a radiograph. 3D microscopy (or tomography) can be computed from a set of radiographs acquired with many different sample orientations. This non-destructive 3D probe was enabled by Feldkamp *et al.* [5] in 1984 when they presented an algorithm to reconstruct a 3D volume (or tomogram) from a set of 2D radiographs taken with a circular X-ray source scanning trajectory. The reconstruction technique developed by Feldkamp-Davis-Kress is analytical, a technique known as filtered back-projection (FBP), and denoted here as FDK-FBP. Reconstruction is only approximate since a circular trajectory does not satisfy the Tuy data sufficiency condition [6]. For *faithful* 3D microscopy, CBCT geometry in this case is restricted to a small cone-angle (see Fig. 1); the limiting angle depends on material structure and is typically less than $\pm 5°$. Never-the-less, this is a very simple and robust technique that is still used today in the majority of commercial CBCT microscopes.

Lab-based micro-focus X-ray sources typically produce near-isotropic X-ray flux in the forward direction; the low-cone-angle geometry required for circular scans means only a small fraction of these X-rays are utilised. Measurements are lower flux when compared with high-cone-angle imaging. This leads to a lower signal-to-noise ratio (SNR) for a given experiment time. In order to perform high-fidelity imaging with a high-cone-angle geometry, a scanning trajectory that satisfies the Tuy condition and enables theoretically-exact tomographic reconstruction is required. An ideal trajectory is helical since there exists an inversion formula of the FBP type developed by Katsevich in 2002 [7]. Katsevich FBP (KFBP) has been utilised in CBCT microscopes developed at the Australian National University (ANU) that incorporate helical scanning with large cone-angles ($\pm30°$) since 2010 [8]. This yields greater than a 40-fold increase in flux when compared with an equivalent circular scan. In order to produce high-fidelity, high-resolution tomograms from a helical scanning trajectory using KFBP at ANU, several issues had to be overcome (as summarised in [9]). In the process of this work, some fundamental drawbacks of the helical trajectory were also revealed [10].

A major shortcoming is the non-uniformity of resolution within the tomogram. This arises in a high-magnification fine-focus geometry where geometric magnification across the sample varies significantly (e.g., a factor of three for a cone-angle of $60°$). Regions of the specimen that are (on average) closest to the source have a much higher magnification than regions that are furthest. Trajectories that provide a greater uniformity in the *average* distance from the source to each tomogram voxel reduce this effect; double helix [10] and low-pitch helix (such as 3PI e.g., [11]) trajectories achieve this at the cost of increased data redundancy and additional overscan (i.e., the additional data required as the X-ray source trajectory scans past the ends of the specimen volume of interest).

Analytical reconstruction schemes, e.g., FBP inversion schemes for helical scanning [7], [12], require that the varying degrees of redundancy in the measured data per voxel of the tomogram be taken into account. This is typically achieved by applying an apodisation or window function to each radiograph to remove unwanted redundancy; for a helical trajectory this is the Tam-Danielsson (TD) window [13], [14]. For large-cone-angle geometries with square detectors, windowing leads to about half the measured data being ignored. Additionally, the problem of inversion from a helical trajectory with this minimal data (as defined by the TD window) is more poorly conditioned than that for the circular trajectory which has a uniform factor-of-two redundancy. Inversion is complex and highly sensitive to specimen/component motion [15], sampling imperfections [16], [17], and component misalignment [18].

Analytical reconstruction schemes impose strict requirements on the input data: it must be linear projected attenuation that is geometrically aligned with a precise continuous trajectory. In practice, measured data is noisy and discretised (with inconsistent pixel response), finitely sampled along an imperfect trajectory with component misalignment and may have beam-hardening and little signal through high-density minerals. A significant amount of pre-processing of the measured radiographs is therefore required. Many of these pre-processing steps are performed as optimisations and require iteration, i.e., forward and/or back-projection, incorporating a physical model of the phenomenon, e.g., beam-hardening correction [19], geometric component alignment [20], component motion correction [21]. Even when highly optimised, this cumbersome preprocessing can easily take longer than the final analytical reconstruction.

Iterative reconstruction (IR) schemes can incorporate physical models, geometry and noise into the forward process, thereby simulating the experiment [22]. They can converge on solutions with reduced artifacts, in particular, those satisfying certain *a priori* information, e.g., [23]. Iterative reconstruction schemes are not restricted to continuous line trajectories since they do not require differentiation of data like their analytical counterparts. In fact, IR is the method of choice for non-ideal, noisy, sparse, or limited-angle measured data such as in positron emission tomography (PET), single-photon emission computed tomography (SPECT), and electron tomography. In these cases, extremely robust but slowly converging statistical reconstruction algorithms are required such as maximum-likelihood expectation maximisation (MLEM) [24] or the simultaneous iterative reconstruction technique (SIRT) [25]. Conversely, for large, low-noise data sets typical of CBCT in the materials and geological sciences, convergence speed must be prioritised; robustness must come through the properties of the trajectory used to collect the measured data. Our objective is the production of high-resolution, high-fidelity tomograms from large CBCT data sets through a computationally efficient IR scheme.

Assuming the employment of some iterative reconstruction scheme, we require a trajectory (not necessarily limited to a continuous line) that: 1) satisfies the Tuy data sufficiency condition with a minimal number of projections (to enable high-SNR imaging), 2) requires minimal windowing to fully utilise the measured data, 3) is maximally isotropic, i.e., provides as uniform resolution as possible, 4) is as well-conditioned as possible, i.e., maximum mutually independent information, and 5) minimum sensitivity to geometric misalignments. In this paper we present such a trajectory, referred to as the *space filling trajectory* (SFT). We also demonstrate how the isotropic nature of the trajectory can be leveraged to achieve rapid convergence in iterative tomographic reconstruction.

The remainder of this article is organized as follows: The space-filling trajectory is defined in Section II and the fulfillment of some of the above requirements is presented in the following sections. Data sufficiency of the SFT is explored in Section IV. The isotropic nature and associated properties of the SFT are outlined in Section V. It is demonstrated in Section VI that the SFT maximises mutually-independent information. This enables a maximum tomogram quality from a given scan time. The sensitivity of the SFT to inconsistencies introduced by geometric and projected-attenuation inaccuracies is investigated in Section VII. The implications of this for automatic a-posteriori geometric system alignment are also presented. Finally, some concluding remarks are included in Section VIII.

II. SPACE-FILLING TRAJECTORIES (SFT)

For low-cone-angle CBCT, circular trajectory acquisition can produce tomograms (using FDK-FBP) of reasonable fidelity,
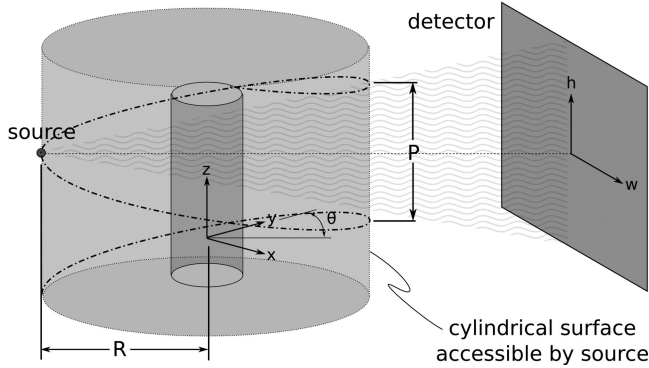
Fig. 2. Depiction of the cylindrical surface, of radius R about the sample rotation/translation axis, accessible by the X-ray source. A helical path with pitch P has been overlaid on this surface as an example trajectory.
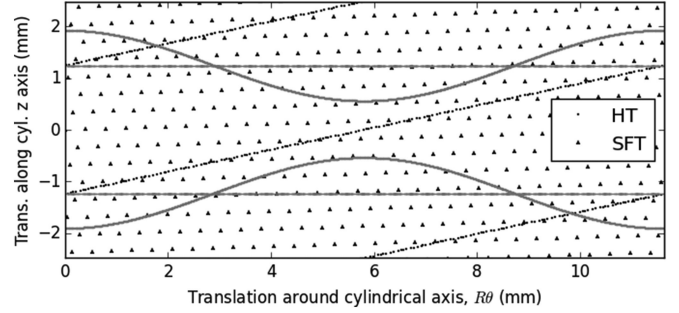

Fig. 3. The space of possible X-ray source positions, i.e., the surface of a cylinder with radius $R = 1.85$ mm (system geometry is described in Section III-B). The squares depict a helical trajectory with maximum pitch calculated according to (5). The triangles depict the proposed space-filling trajectory with Z calculated according to (2).

despite only the central tomogram plane, (in which the source points are located), being theoretically exactly reconstructible. In this context, "theoretically exact" means the reconstruction problem has a unique solution for noiseless data. The circular trajectory involves rotation of the source and detector (or equivalently, the specimen) about a single point and single axis. For high-cone-angle CBCT, the circular trajectory becomes inadequate as tomogram fidelity rapidly diminishes with distance from the central tomogram plane. Theoretically exact reconstruction requires an X-ray source scanning trajectory that involves motion in another dimension. This is commonly achieved by translation of the specimen (or equivalently, the source and detector) parallel to the rotation axis. The trajectory rotation and translation degrees of freedom yield a 2D space of possible X-ray source positions. These source positions lie on the surface of a cylinder with radius R — the source-to-rotation-axis distance (see Fig. 2). The co-ordinate $(z, R\theta)$ specifies a point on this cylinder surface, where z is the translation parallel to the rotation axis and θ is the rotation angle.

The major innovation of this work is to consider CBCT scanning trajectories not as a continuous curve but rather as a set of distinct points placed in the space through which the source point can move. Within this framework it is natural to consider trajectories for which the source points are distributed in a uniform manner throughout the space. We call this type of trajectory a *space filling trajectory* (SFT). Fig. 3 plots source points from a SFT (black triangles) and traditional helical trajectory (HT) closely-sampled source points (black dots). The system geometry used to generate this figure is described in Section III-B. Here however, we have used a detector binned by eight, i.e., pixels-per-side $M = 600/8 = 75$. Therefore, the reconstructed volume is $N = 68$ voxels in the plane normal to the rotation axis, and $E = 96$ projection images are required to reconstruct each voxel. The HT has $\Omega = 375$ source points, and the SFT has $\Omega = 286$.

There are two drawbacks when deviating from a closely sampled continuous path. The first drawback is that the acquisition protocol necessarily contains "dead time" as the system moves to each new X-ray source position. This is a limitation when rapid imaging is required, such as capturing dynamic processes, (e.g., flow, compression, dissolution). However, due to the low

X-ray flux emanating from a micro-focus source in a typical microscopic CBCT application, the required "dwell time" at each source position to achieve a reasonable SNR is considerable and this dead time becomes insignificant. The second drawback is that tomograms must be computed using iterative reconstruction (IR), since the differentiation required along the trajectory curve in analytical inversions can no longer be approximated by finite difference. This means that the ability for rapid turnaround from experiment to 3D volume is limited due to the increased computational requirements of IR. However, as stated in the introduction, IR enables more physics-based *a priori* information to be incorporated into the reconstruction process, and can achieve a quantitative volume with greater fidelity than traditional analytical inversion, (see e.g., [26]).

There are numerous practical ways to uniformly sample the space of the cylindrical trajectory surface, some of the simplest being: a regular grid and pseudo-random points [27]. However, the source trajectory should also satisfy a discretized form of the Tuy [6] sufficiency conditions in order to guarantee the possibility of a theoretically exact reconstruction. The following Section II-A establishes bounds on the SFT sampling density (step size) based on the Nyquist sampling theorem. Section II-B then describes the SFT realization (low discrepancy sampling of a helix) that is considered for the remainder of the paper. Subsequently, in Section IV we computationally illustrate that our low discrepancy helix sampling (subject to the Nyquist sampling density) satisfies the discretized interpretation of the Tuy sufficiency conditions.

A. Space-Filling Trajectories for Large-Angle CBCT

For the continuum cone beam tomography inverse problem, Tuy [6] derived an analytic reconstruction formula which imposed a set of weak conditions on the "source trajectory" (*bounded curve*) that ensured acquisition data was sufficient for a theoretically exact reconstruction. For the discrete inverse problem, there is yet to appear in the literature an equivalent to the Tuy trajectory conditions. Instead, for discrete/digitally acquired (band-limited) radiograph data and digital tomogram reconstruction, we use Nyquist sampling arguments in order to calculate bounds on the z and $R\theta$ sampling density (step sizes) of the space-filling trajectory discretization. These

step-size bounds are dependent on the acquisition geometry and the detector discretization.

Let L denote the *source-detector-distance*, and W and H specify the detector *width* and *height* respectively. The radius of support, (or limiting radius of the specimen), is found as $r = RW/2\sqrt{L^2 + (W/2)^2}$. Given a pixel size p, the highest frequency of the measured data is $1/2p$ at the detector; this corresponds to $L/2Rp$ at the rotation axis (or specimen). To maximise tomographic resolution, the Nyquist sampling theorem dictates that the source points sample the z-direction with a minimum frequency of L/Rp.

The angular-space variant of Nyquist sampling commonly used in tomography is the Crowther criterion [28]. This requires that the minimum number of angular samples for reconstruction of an $N \times N$ array is $\pi N/2$, i.e., an angular frequency of $N/4$. Typically N is specified as $N = W/p$ (although for very large fan angles $N = 2rL/Rp = WL/p\sqrt{L^2 + (W/2)^2}$ is more appropriate); the sampling frequency becomes $W/4p$.

Traditional helical and saddle acquisition trajectories (among others) can be calculated to satisfy these sampling requirements. Additionally, one can enhance traditional trajectory sampling to possess space-filling properties, some enhancements include

1) reordering of the angular positions in a helical trajectory [29], [30];
2) multi-helix, i.e., generalisation of double helix [10];
3) low-pitch helix [30].
4) reordering of the angular positions in a saddle trajectory;
5) multi-saddle, i.e., stacked or interleaved vertically;
6) high-frequency saddle [31];

The space-filling trajectory sampling considered in this paper is produced by stepping along an extremely low-pitch helix. Indeed, enhancements A-F can be described (or closely approximated) in this manner. For the remainder of the paper, the SFT is generated using a low-discrepancy sequence of strides along a low-pitch helical path. The generation of this sequence is described in the next section.

B. A Low-Discrepancy Space-Filling Helix

Let E denote the number of projection images (or radiographs) in an *ensemble* required to exactly reconstruct a tomogram voxel. Let Z denote the vertical translation attained while collecting E radiographs. Let Q define the number of radiographs (or source points) per revolution. For circular trajectories $E = Q$ in the source rotation plane. However, for helical and space-filling trajectories E and Q are distinct. A trajectory with Ω source points and starting at position $(z_0, R\theta_0)$ is defined as:

$$\{(\omega Z/E, \omega 2\pi R/Q) + (z_0, R\theta_0) : \omega \in [0, \Omega]\}. \quad (1)$$

Here, we use the quantity E to enforce the satisfaction of the Tuy data sufficiency criterion. For practical acquisitions, we are yet to determine expressions that yield optimal values for E, Z, and Q that sample the cylindrical surface as uniformly as possible and also satisfy the vertical and angular sampling bounds of the previous section. However, in the following, we calculate bounds for Z and Q (and subsequently E) based on the previous Nyquist sampling density bounds and the number

of source positions for which a ray intersects both a tomogram voxel and the detector.

The number of radiographs containing the projection of a point in the tomogram varies depending on the position of the point in the tomogram. This has been illustrated in Fig. 3, where the region between the dashed grey lines bounds the source points for which the ray through the central tomogram voxel intersects the (finite sized) square detector. The region between the solid grey lines in Fig. 3 shows the source points where the ray through a single edge voxel (from the central tomogram plane at radius r from the rotation axis) intersects the same square detector.

To define Z conservatively, such that no voxel is under-sampled, we require that all voxels project to at least E consecutive radiographs, i.e., an ensemble of radiographs. This is equivalent to finding the shortest distance between the solid grey lines in Fig. 3 and is found as:

$$Z = \frac{H(R - r)}{L}. \quad (2)$$

Observe that the area between the grey lines (solid or dashed) in Fig. 3 is constant regardless of voxel location; removing the "consecutive" restriction above, $Z = HR/L$ produces fewer redundant ray paths but has some proportion of voxels projecting to fewer than E radiographs. However, we will use Eqn. 2 when exploring SFT properties by simulation. The set of E source positions ordered by height must have a vertical stride no greater than pR/L, i.e., $EpR/L \geq Z$ or $E \geq H(R - r)/Rp$. Similarly, the set of positions ordered by angle must have an angular stride no greater than $4p/W$, i.e., $E4p/W \geq 2\pi$. Therefore, we have the lower bound on E:

$$E \geq \max\left\{\pi W/2p, \frac{H(R - r)}{Rp}\right\}. \quad (3)$$

Uniform coverage of the source point plane can be achieved with source positions which lie at the vertices of a regular triangular tessellation, i.e., $P = \sqrt{3}\pi R/Q$ and $\mathrm{frac}(Q) = Q - \lfloor Q \rfloor \approx 1/2$. Of course if $\mathrm{frac}(Q) = 1/2$ then only $2Q$ unique angles are sampled. We desire a $\mathrm{frac}(Q)$ that is not equal to, or approximated by, a rational fraction with a small denominator (relative to the number of revolutions). An ideal value for generating low-discrepancy sequences is the golden ratio $\phi = (\sqrt{5} - 1)/2 \approx 0.618$. The partitioning properties of the residual $2\pi\phi R/Q$ on the range $(0, 2\pi R/Q)$ provide an approximately uniform angular sampling with each new sample dissecting the current largest partition. The number of radiographs per revolution, Q is then found as:

$$Q = \left\lfloor \sqrt{\frac{\sqrt{3}\pi ER}{Z}} \right\rfloor + \phi. \quad (4)$$

The next Section III outlines the experimental method of simulation. The following Section IV numerically demonstrates that this SFT satisfies a discretized form of the Tuy data sufficiency condition. The remainder of the paper uses simulation to explore the properties of this trajectory along with demonstrations of the implications of these properties.
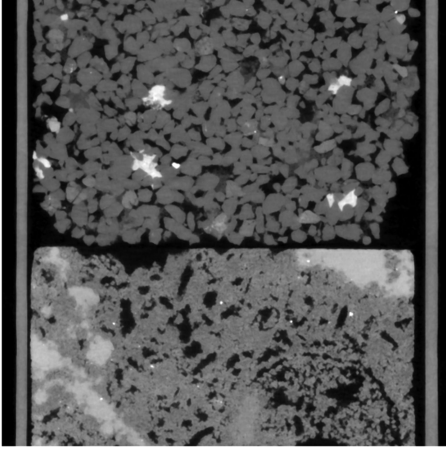
Fig. 4. Central 2D slice, $x = 0$, through the 3D sandstone/limestone phantom. Greyscale window: [black = 0.0 mm^{-1}, white = 1.0 mm^{-1}].

III. EXPERIMENT SIMULATION

Since much of the exploration of the properties of the SFT are through simulations, we will first present the details of how these simulations were performed. Here we describe the phantom utilised, the experiment simulation (forward-projection) procedure performed with various scanning trajectories, and the noise model used.

A. Sandstone/Limestone Phantom

This phantom has been generated from a reconstructed tomogram of stacked sandstone and limestone rock cores as depicted in Fig. 4. The original volume was vertically truncated to become cubic, and sub-sampled to $N = 512$ voxels per side with a cubic voxel dimension of 4.11 μ m. The attenuation values ranging from 0.0 to 1.0 mm^{-1} were binned into 12 equally spaced discrete values.

B. Simulation Geometry

Unless otherwise stated, the specimens are placed at $R = 1.85$ mm from the X-ray source (i.e., source-specimen-distance), a $W \times H = 400 \times 400$ mm^2 detector is located $L = 300$ mm from the source (i.e., source-detector-distance). This gives a large cone-angle of 67.38°. Reconstructed voxel size is calculated as detector pixel size scaled by $R/L = 0.00617$, equivalently given the detector is $M \times M$ pixels, voxel size $= WR/ML$. The limiting radius of support is $r = RW/2\sqrt{L^2 + (W/2)^2} = 1.0262$ mm. The diameter (and thus reconstruction domain) in voxels is $N = ML/\sqrt{L^2 + (W/2)^2} = 0.832M$. We use $M = 600$ as a typical geometry. This yields $N = 500$, and the number of radiographs $E = \pi N/2 = 784$; however, to make this suitable for under-sampling, we select $E = 768$. The specimen height dimension is 2.0524 mm, i.e., N voxels, giving an N^3 voxel reconstruction.

Note that in order to simulate physical X-ray cone-beam integrals (as opposed to unrealistic line-integrals) and avoid the inverse crime, the forward-projection data was calculated with a $3M \times 3M$ pixel detector that was rebinned to $M \times M$ pixels. It is worth noting at this point that the projection and back-projection operators used in our code are not exactly adjoint. The projection process steps through the volume along each line of integration and sums the result of tri-linear interpolation at regular intervals along this line; the back-projection process sums the result of bi-linear interpolation of the projection-images at the projected voxel position.

a) Circular trajectory: by definition $Z = 0$, and we use $Q = E = \Omega = 768$. Note that $L = 300$ mm gives a large cone-angle which invalidates the pseudo-parallel-beam requirements, so we have used $L = 1200$ mm in many cases. Note that this increase in L by four increases required exposure time by 16 (which is relevant for the noise calculations in Section VI-B.).

b) Helical trajectory: in order to minimise redundancy, we use the maximum pitch (or vertical translation per rotation), P, according to equation 5 from [18]:

$$|P| \leq \frac{\pi RLH}{((W/2)^2 + L^2)(\pi/2 + \arctan W/2L)}. \qquad (5)$$

Given the above parameters, this is defined as $P = QZ/E$. From the simulation geometry used here we calculate $P = 2.485$ mm. Since each point is reconstructed from PI-lines, (i.e., approximately half a revolution of data), we set $Q = 2E$ and therefore $Z = 1.243$ mm; for overscan we use the conservative estimate presented in [18] of an additional $\pi/4 + 3\alpha_f$ rotation at each end, where α_f is the fan-angle; this gives $\Omega = 3.897E = 2993$.

c) Space-filling trajectory: we use $Z = 1.098$ mm calculated according to (2); Q is calculated according to (4); an overscan of $E/2$ radiographs is used at each end of the trajectory to ensure all voxels project to at least E radiographs; this gives $\Omega = 2.977E = 2286$.

C. Poisson Noise

Noise has been included in Figs. 9(c) and 10 in accordance with [32]. Here, noise is parameterised solely by exposure time, t in seconds. A mean X-ray energy of $\xi = 30.0$ keV is used, with a typical scaling factor (that encompasses, for example, luminescent conversion efficiency and electronic gain) of $\tau = 0.016$. We define measured intensity to be $\gamma = 1024$ intensity units (IU) per second, according to $\gamma = n\xi\tau$, where n is the number of detected photons. Assuming a Poisson distribution, the variance of measurement is $\sigma^2 = n\xi^2\tau^2$. We have also included *dark current* noise assuming a normal distribution with a typical value $\sigma_d = 24$ IU.

IV. DATA SUFFICIENCY OF THE SPACE-FILLING TRAJECTORY

As outlined in the introduction, not all scanning trajectories provide sufficient information for a theoretically-exact reconstruction. For the continuum tomography inverse problem, source trajectories which satisfy the Tuy sufficiency criterion [6] ensure a theoretically exact reconstruction is possible. The essence of this criterion stipulates that a trajectory is sufficient if all planes that intersect the reconstruction volume also *cut* the source trajectory. Of course, the Tuy condition is only applicable for continuous source trajectories. For discretely sampled

trajectories, the continuum is traditionally approximated by using angular step-sizes which are at or below the Crowther criterion [28], i.e., the angular spacing between adjacent source points is comparable to the angular spacing between adjacent detector pixels. Theoretically exact reconstruction schemes (e.g., of the FBP type) also require such dense sampling along the acquisition path in order to perform differentiation, but iterative reconstruction methods liberate us from this constraint. The distributed sampling of the SFT, by design, means there exists no such continuous curves that can represent the trajectory.

Development of a method to apply the Tuy condition to discrete sets of vertices (source positions) is an ongoing problem. It was first considered by Noo *et al.* [27] for the strided helix, multi-circle and a pseudo-random distribution of source points. They devised a parameter ϵ, the furthest distance of any plane to the nearest vertex, but found it wasn't necessarily indicative of tomographic resolution. Many subsequent attempts to extend this analysis have been made, particularly in the field of SPECT, with limited success. Here, we demonstrate data sufficiency for a small example SFT by presenting the 3D Radon transform (RT) of the trajectory with the same discrete resolution used in reconstruction. The value at each point in 3D Radon space, at $\mathbf{x} = (x, y, z)$, is determined as the integration of the volume over the plane through $\mathbf{x}$ that is normal to the vector from the origin to $\mathbf{x}$. The 3D RT yields precisely the set of plane integrals required to test the Tuy condition (although the effect of a finite detector is ignored).

We set up a set of source points in a discrete (gridded) volume by placing a delta function at each source point and tri-linearly interpolating to the nearest voxels. Circular, helical, and space-filling trajectories have been simulated for comparison with $M = 140$ m thus $N = 116$ voxels and $E = 180$; Here the circular trajectory used $\Omega = E$ while the HT and SFT both used $\Omega = 4E$. We define a spherical region of support (or reconstruction domain) within this plotted trajectory. If every point of the 3D Radon transform computed for each *trajectory* volume is greater than 0.5 within the sphere then all planes, of thickness one voxel (the spatial sampling required), through the domain contain at least one source point. The 3D Radon transform of each trajectory is presented in Fig. 5. Red indicates the boundary of the spherical support. Blue indicates a plane sum below 0.5. The well known solid torus of data sampling for the circular trajectory can be observed with data missing in the z direction. Both the helical and space-filling trajectories have complete data inside the spherical support. Due to the symmetrical nature of the SFT, we observe a more uniform distribution of redundancy.

V. ISOTROPY OF THE SPACE-FILLING TRAJECTORY

A. Resolution and Signal Uniformity

A helical scanning trajectory is anisotropic, i.e., highly non-uniform when viewed from the perspective of a point (or voxel) within the object [10]. Regardless of windowing, the number of source points where each voxel projects onto the detector area [Fig. 6(a-i) and (a-ii)] and the average distance to the source [Fig. 6(b-i) and (b-ii)] varies considerably.
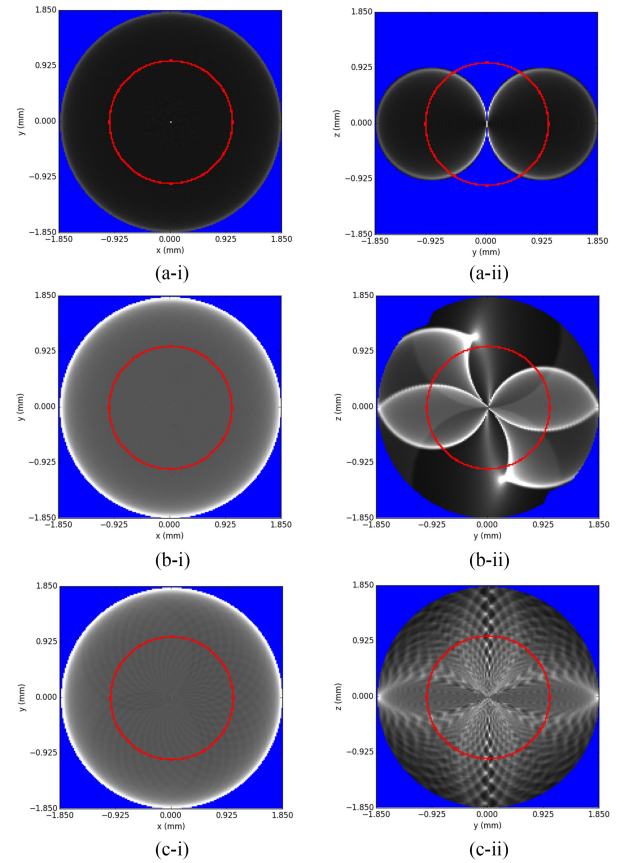

Fig. 5. Horizontal (i) and vertical (ii) slices through Radon space, determined by taking the 3D Radon transform of discrete sets of source points. Greyscale window: [black = 0, white = 8]. Geometry specified in Section III-B. (a) Circular trajectory, (b) helical trajectory, and (c) space-filling trajectory. Only Radon data out to $R = 1.85$ mm (85 px) was calculated, the extent of spherical region of support (i.e., reconstructed domain) is red. Blue indicates plane sums ≤ 0.5.

In the large cone-angle fine-focus geometry considered here, non-uniform source distances leads to non-uniform resolution in the reconstructed volume when under high-magnification. Average magnification is computed as L/R, however, we have an expanding cone beam with magnification of regions of the sample close to the source being $(R - r)/L$ and far from the source being $(R + r)/L$. Thus sample regions that are on-average close to the source are projected with better resolution than regions that are far on-average. The SNR of a reconstructed voxel improves with the number of source points that project that voxel onto the detector area. A large variation in this number across the volume leads to a large variation in tomogram SNR.

In contrast to the anisotropy of the helix, the number of source points where each voxel projects onto the detector area for the SFT [Fig. 6(a-iii)] and the average distance to the source [Fig. 6(b-iii)] is isotropic and as uniform as can be achieved with standard CT imaging configurations.

B. Point-spread-function (PSF) Uniformity

In fact, the SFT is maximally isotropic assuming the source is restricted to lie on the surface of a cylinder. This is quite distinct
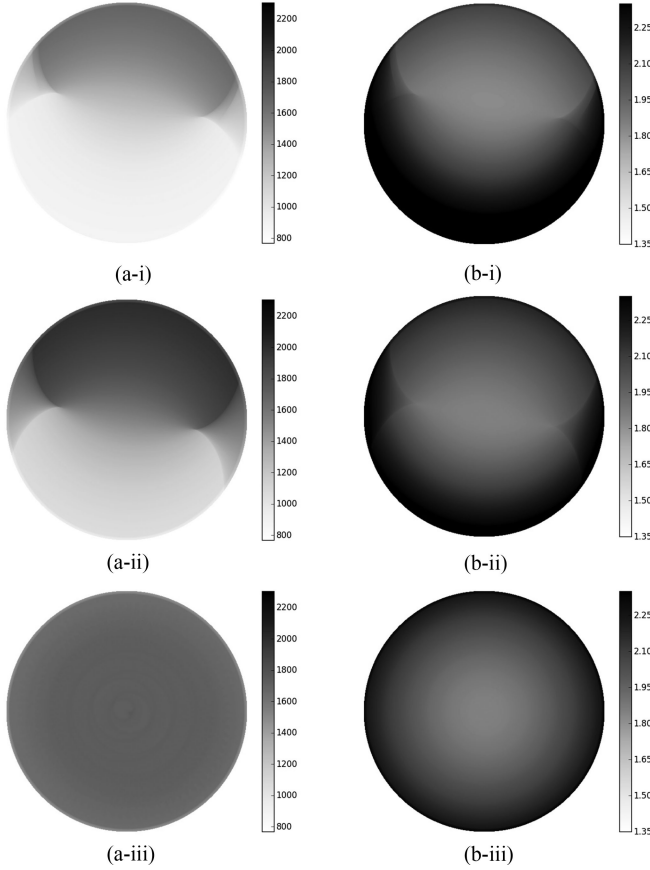
(a-i) (b-i)

(a-ii) (b-ii)

(a-iii) (b-iii)

Fig. 6. Central 2D horizontal (i.e., XY-plane) slice through the reconstruction volume showing (a) number of X-ray source positions that back-project through each voxel, and (b) the average X-ray source distance, for the (i) helical trajectory with Tam-Danielsson window applied, (ii) un-windowed helical trajectory, and (iii) space filling trajectory. Geometry is given in Section III-B. Note that $E = 768$ and *source-specimen-distance* $= 1.85$ mm.

from continuous path trajectories where the blurring from back-projection is highly anisotropic and location dependent: for the SFT the directions of the set of measured rays passing through each voxel in the tomogram are as uniformly distributed on the unit sphere as is possible within the constraints of the imaging apparatus, and with little potential for improvement with other imaging configurations.

Even for the SFT, the range of directions of the set of measured rays passing through a given voxel depends on the location of that voxel within the reconstructed volume. This is due to the limited acceptance-angle dictated by the finite detector height. A voxel in the center of the volume (i.e., on the rotation axis) is projected onto the detector area from source points in all directions equally well. An example of this is presented in 3, the set of source points in the region between the grey dashed lines project the central voxel to the detector area. In contrast, the set of source points that project an off-axis voxel to the detector area is shaped by a sinusoidal envelope. For a voxel position (x, y) in the plane, the amplitude of the sinusoid is determined by radius ($\sqrt{x^2 + y^2}$), while the phase is determined by $\tan^{-1}(y/x)$. Fewer near-side source points project the voxel to the detector area than far-side source points due to the finite detector height. An example of this scenario is also presented in Fig. 3, the source
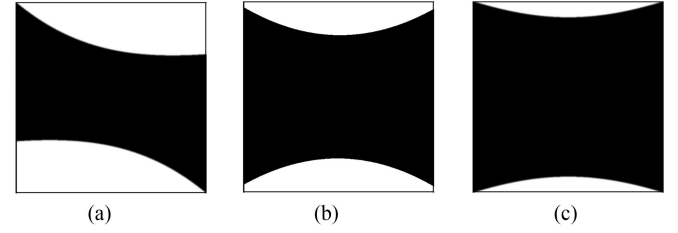

Fig. 7. Apodisation functions, or windows, that may be applied to radiographs: (a) Tam-Danielsson window for the HT, and (b) n-PI window for the SFT assuming it is a low-pitch HT, to remove redundancy; (c) Colsher window for the SFT to equalise the acceptance angles for each reconstructed voxel. System geometry specified in Section III.

points in the region between the solid grey lines project a voxel at maximum radius onto the detector area. The area enclosed by the sinusoidal envelope is unchanged by phase or amplitude, so the total number of source points that project all voxels onto the detector area is approximately constant [as can be seen in Fig. 6(a-iii)]. A source point cropped on the side near to the voxel is compensated by an additional source point on the side far from the voxel (180° apart). The principal consequence of this symmetry is that an unfiltered backprojection of linearised radiographs, to a decent approximation, results in shift-invariant blurring of the volume.

C. Leveraging Isotropy for Effective Pre-Conditioning

Shift-invariant blurring can be inverted using deconvolution (an operation similar to ramp-filtering in FBP). In 1980, Colsher [33] analysed the case of idealised positron emission tomography (PET) data and proposed reconstruction algorithms of the back-projection filtration (BPF) and FBP type with shift-invariant spatial filtering. X-ray transmission data collected using an SFT is similar to PET, except that (a) the SFT contains a distinct source position per radiograph where each data point in PET has a distinct source point, and (b) the SFT, based on a standard CT configuration, has a planar detector. An apodisation function (or window) can be applied to the radiographs to simulate a cylindrical detector by enforcing a constant acceptance angle as assumed for the inversion by Colsher in [33]. This will be referred to as the *Colsher* window, defined as:

$$C(w) = \pm (H/2) \sqrt{\frac{L^2 + w^2}{L^2 + (W/2)^2}}. \qquad (6)$$

This is depicted in 7 for the experiment geometry described in Section III-B. Fig. 7 also shows the Tam-Danielsson window for a HT for comparison. The generalisation of this for a low-pitch HT known as the n-PI window [34] is also presented for the SFT. Note that these windows are designed to reduce unwanted redundancy rather than restrict X-ray detection to a constant acceptance angle. Colsher or n-PI windowing are not strictly necessary for IR but cause the SFT to have higher symmetry more amenable to the accelerated IR methods discussed below. For a typical geometry used at the ANU micro-CT labs with a fan angle of 60°, Colsher and n-PI windows for the SFT removes only ∼15% and 25% of data respectively compared with ∼ 50% removed by the Tam-Danielsson window for the HT.
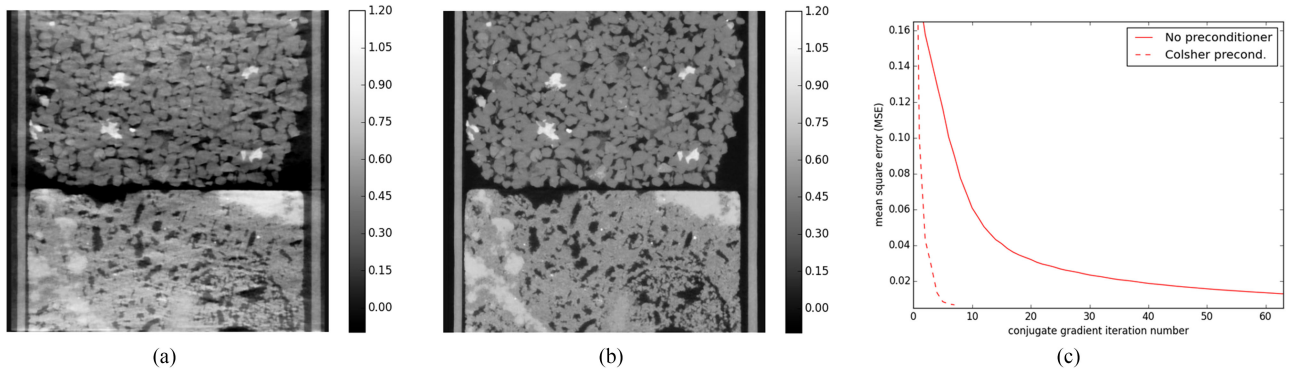
Fig. 8.   Vertical 2D slices through the sandstone/limestone phantom, reconstructed from a space filling trajectory, $Z = HR/L = 2.47$ mm, $\Omega = 1400$, with (a) Backprojection with Colsher filtering, (b) 8 iterations of Colsher-filter pre-conditioned CGM. Acquisition details are in Section III-B; both (a) and (b) use Colsher windowing of projections.

We recall that iterative methods are required to reconstruct the sparsely sampled SFT projection data. In order to *pre-condition* and accelerate convergence we can incorporate Colsher filtering in the radiographs. We model data acquisition as a linear process:

$$\mathbf{A}\mathbf{x} = \mathbf{b},$$

where $\mathbf{b}$ is the measured data, $\mathbf{x}$ represents the object attenuation (our objective function), and $\mathbf{A}$ describes X-ray projection. Back-projection is the adjoint of projection, $\mathbf{A}^T$. Applying back-projection to the measured data, $\mathbf{A}^T\mathbf{b}$, recovers a heavily low-pass filtered form of $\mathbf{x}$. This can be significantly improved by applying Colsher filtering and windowing. Let $\mathbf{F}$ be the Colsher filtering applied in the projection domain; let $\mathbf{W}$ be a diagonal matrix giving the Colsher windowing function. Fig. 8(a) depicts the result of $\mathbf{A}^T\mathbf{W}\mathbf{F}\mathbf{b}$; it is a far better approximation to $\mathbf{x}$ than that from simple back-projection. However, it contains some artifacts since F is a shift invariant approximation to $(\mathbf{A}^T)^{-1}\mathbf{A}^{-1}$. Note that $\mathbf{F}$ is a self-adjoint circular convolution that can be applied very efficiently as a multiplication in Fourier space. This filtering technique can be used as a pre-conditioner to speed up a conjugate gradient method (CGM) iterative reconstruction.

In a tomography context, CGM seeks to find the most likely function $\mathbf{x}$ assuming a Gaussian distribution in the measured data $\mathbf{b}$ according the the model:

$$\mathbf{A}^T\mathbf{A}\mathbf{x} = \mathbf{A}^T\mathbf{b}.$$

Inserting filtering and windowing as a pre-conditioner, we arrive at the following:

$$\mathbf{A}^T\mathbf{W}\mathbf{F}\mathbf{A}\mathbf{x} = \mathbf{A}^T\mathbf{W}\mathbf{F}\mathbf{b}.$$

Although, both $\mathbf{F}$ and $\mathbf{W}$ are self-adjoint, this can not be rewritten symmetrically as $(\sqrt{\mathbf{F}}^T\sqrt{\mathbf{W}}^T)(\sqrt{\mathbf{W}}\sqrt{\mathbf{F}})$ due to the windowing operation. Thus convergence is not guaranteed, however, windowing is beneficial since the filtered data outside the Colsher window is produced using a significant degree of extrapolated data. The result of applying this pre-conditioner in to our simulated data is presented in Fig. 8(b). The convergence plot in Fig. 8(c) shows this simple pre-conditioned CGM (PCGM) gives an order of magnitude speed up in convergence.

Although finding an efficient reconstruction scheme for the SFT is a relatively unexplored problem, this demonstrates that the properties of the trajectory can be leveraged heavily. pre-conditioning can also be applied by Colsher filtering of the post-backprojected volume. A form of this that incorporates multi-grid iterative reconstruction schemes and converges to reasonable quality in just 2 iterations has been presented in [35].

VI. MAXIMISING MUTUALLY-INDEPENDENT INFORMATION THROUGH THE SPACE-FILLING TRAJECTORY

With a large stride between adjacent source points, data collected using the SFT contains information about the specimen that is more mutually independent. The pseudo-hexagonal tiling of the source point plane minimises the area of unpopulated regions and maximises the distance between two *neighbouring* source points. This makes the SFT data maximally independent given the constraints of the imaging apparatus. The *space-filling* concept is optimal in the absence of *a priori* knowledge of the object, as distinct from the method of Stayman and Siewerdsen [36] which determines an optimal trajectory for a particular specimen.

Tomographic reconstruction from projection data is by nature an ill-posed problem [37], however, this SFT property of maximally independent information should lead to a problem that is better conditioned and yield reconstructed tomograms with lower levels of noise and geometric artifacts for a given experimental acquisition time. Proof of this is an open problem; for the remainder of this section we attempt to demonstrate these properties by example.

A. Condition Number

Through research with multi-source X-ray CT systems for security screening, Thompson *et al.* [29], [38], [39] have investigated highly-constrained, discrete source trajectories with properties similar to those proposed here. Their trajectories are limited to a set of fixed X-ray sources and detectors located in a ring around a conveyor belt. The set of sources are offset in z with respect to the set of detectors. They seek to optimise the source firing order, as the conveyor belt runs through the ring, to maximise tomogram quality (or minimise artifacts). Thompson investigated the condition number for these discrete trajectories
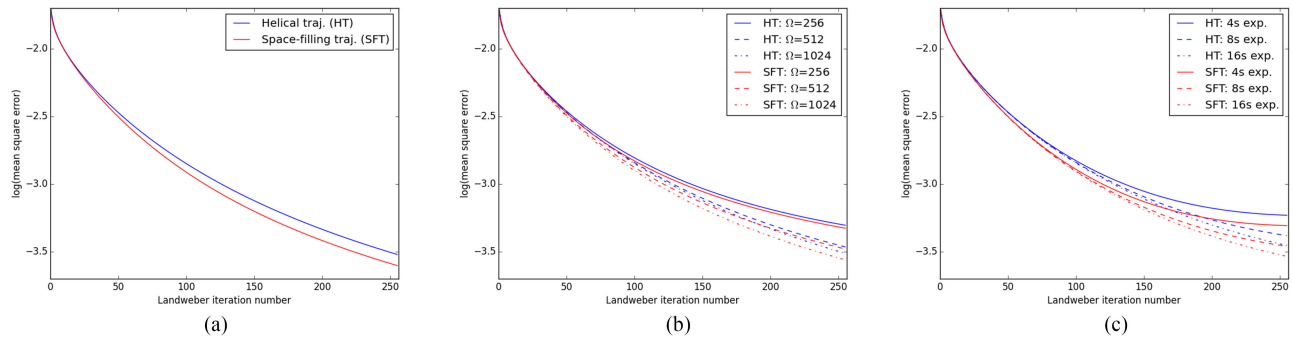
Fig. 9.   Log(MSE) convergence plots of gradient descent IR for HT compared with SFT using geometry specified in Section III-B for a) standard experiment simulations, b) simulations with restricted total number of radiographs, Ω, and c) simulations with various radiograph exposure times (or noise levels). Mean square error (MSE) is calculated compared with the known phantom volume data.

by computing the singular-value-decomposition (SVD) analysis of some small simulations [38] – for larger data sets this analysis is too computationally demanding to be feasible. The condition number can be defined as the ratio of largest to smallest singular values of the forward projection matrix. Thompson investigated the condition number when reconstructing both a single z-slice and 12 slices with varying x/y pixel size, as well as varying the number of z-slices from one to 60 with a fixed x/y pixel size. He found that the lattice trajectory ("k = 35") had a better condition number than the helix trajectory ("sequential") in all cases. He also showed that the singular vectors were much more smooth and symmetric for "k = 35" compared with "sequential".

The speed of convergence for gradient descent algorithms depends on the condition number of the forward-projection matrix. To show that the SFT is less ill-conditioned than the helical trajectory, we reconstruct the phantom from data collected with both HT and SFT using the Landweber algorithm [40] which is a special case of gradient descent. The value used for the Landweber relaxation parameter was $1/EN$; This is typical in computed tomography as it approximates a diagonal rescaling of the problem. Fig. 9(a) presents convergence plots. It can be seen that overall the IR from the SFT data does indeed converge more rapidly, indicating an improved condition number compared with the HT. We also investigated the effects of windowing and removing the "cone-beam" integrals in forward projection (as described in Section III-B). Applying windowing significantly degraded the rate of convergence for the HT with only a slight loss of performance for the SFT. However, for these noise free cases, windowing is predominantly removing additional information, the decrease probably just reflected the proportion of data masked out, i.e., 50% for the HT and 15% for the SFT. Replacing "cone-beam" integrals with line integrals had little effect.

Landweber IR convergence rates for simulated experiments with the total number of source points (or radiographs), Ω, limited to 256, 512, and 1024 is presented in Fig. 9(b). In the simulations we have maintained the ratio of E/Ω compared with that for a full set of radiographs. Here the IR from the SFT data again converges more rapidly than that for the HT, however, the performance benefit seems to reduce for sparser sampling levels. Assuming a Poisson noise model as described in Section III-C, Landweber IR convergence rates for simulated
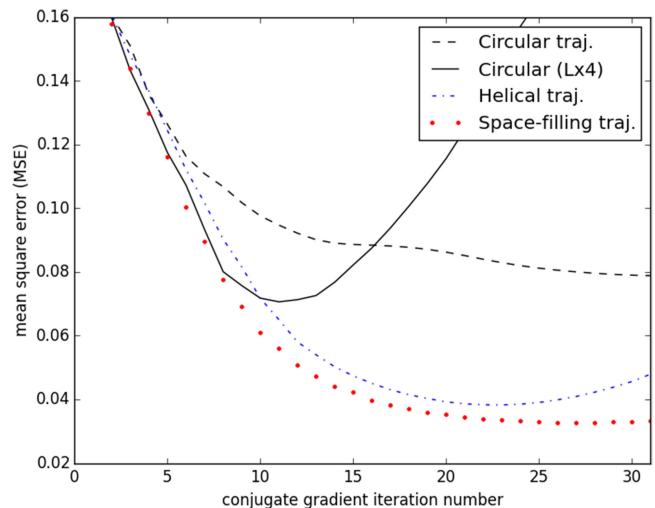

Fig. 10.   Mean square error (MSE) convergence plot for CGM reconstruction of the sandstone/limestone phantom, from data collected over approximately constant experiment time (geometry specified in Section III-B) using circular trajectory, circular trajectory with a long source-detector distance ($L \times 4$), helical trajectory, and space-filling trajectory.

experiments with 4 s, 8 s, and 16 s exposure times are presented in Fig. 9(c). The IR from the SFT data converges more rapidly than that for the HT in all cases. A similar degradation of the convergence plots with increased noise is observed for both SFT and HT data.

B. Improved SNR or Reduced Scan-time and Reduced Data

The SFT satisfies data sufficiency, utilises the entire detector area, and has a better condition number than a HT with less radiographs; it is a very efficient trajectory. Other methods to include redundancy such as double-helix and 3PI helix trajectories require a certain sampling rate along the continuous trajectory and significantly increase the number of radiographs required. Fig. 10 shows the relative performance of circular (with both short and long source-detector distances, L), helical and space-filling trajectories given an approximately constant experiment time. To allow comparison, IR has been performed using the conjugate gradient method (CGM). Convergence plots are given in Fig. 10. Convergence of all data sets is comparable
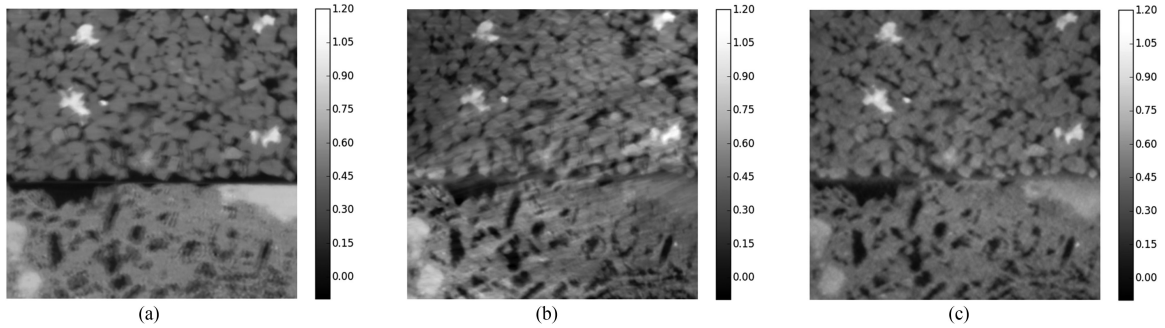
Fig. 11. Subsets of vertical 2D slices through a sandstone/limestone phantom, with misalignments of 2ou in all parameters (as specified in [18]), reconstructed with ramp-filtered back-projection from (a) circular trajectory, (b) helical trajectory, and (c) space-filling trajectory. Geometry is specified in Section III-B.

for the first few iterations. The reconstruction artefacts due to high-cone angle for the circular trajectory give a strangely behaved convergence with the worst MSE ($>$0.08). These artefacts are overcome by using a $4\times$ larger source-detector distance ($L \times 4$), however, this reduces flux by a factor of 16. The high level of noise in this case causes the MSE to diverge quickly with a poor optimal MSE (0.07). The convergence of the HT and SFT data are more well behaved with the SFT providing the highest fidelity tomogram, i.e., the lowest MSE (0.033 compared with 0.04), from fewer projections.

VII. SENSITIVITY OF SPACE-FILLING TRAJECTORY

A. Sensitivity to Component Misalignment/Motion

The SFT is insensitive to perturbation of the input data, i.e., it is relatively well behaved when components (or the specimen) are misaligned, or under specimen/component motion during scanning. This is a very important property in practice. Kingston *et al.* determined a referenceless post-acquisition software alignment protocol for the circular trajectory [20]. Due to its redundancy, the circular trajectory is also insensitive to perturbations and misalignment of radiographs manifests as blur in the tomogram. The alignment protocol is robust since blur is easily detected, quantified, and minimised. In contrast, Varslot *et al.* showed that given the helical trajectory with Katsevich filtering, it is quite difficult to align using this protocol [18]. The reason for this is that the HT has no redundancy and is sensitive to perturbations [15], misalignment introduces geometrical distortions and disjoint features. This was mitigated in [18] by employing horizontal ramp-filtered back-projection with no Tam-Danielsson window applied when scanning for alignment parameter values. Redundancy is then introduced leading to increased blurring as desired, however, we note that some streaking is still present. These streaks make it very difficult to align helical data using sharpness measures.

As for the circular trajectory, the isotropic nature of the SFT causes misalignment of radiographs to degrade the tomogram as blur when using horizontal ramp-filtered back-projection. It is an ideal trajectory for software alignment that maximises sharpness in the tomogram (as in [20]). Using the parameterisation and optimal units (ou) defined in [18], Fig. 11 shows the reconstruction from by ramp-filtered back-projection for a circular, helical, and space-filling trajectory, given a misalignment of
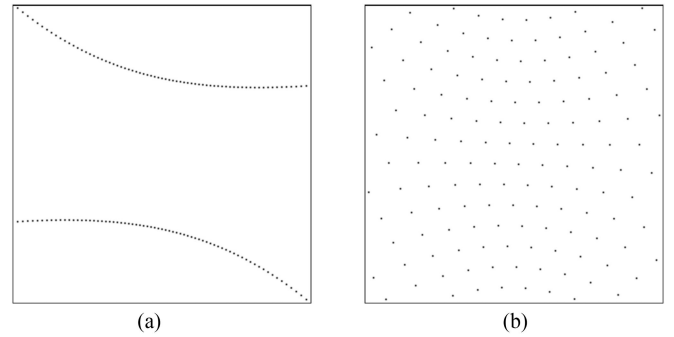

Fig. 12. An example of the position of all PI-line X-ray paths on a radiograph given the geometry described in Section III-B for (a) helical trajectory, (b) space filling trajectory.

the radiographs of 2ou in each parameter. The behaviour under misalignment from each trajectory (as described above) is quite evident.

Alignment can also be performed by minimising the PI-line difference in the projection data [41]. PI-lines are points on the radiograph where the X-ray source is positioned elsewhere in the trajectory. Thus, there exists an X-ray path with an equivalent but opposite trajectory on a different radiograph that should have the same (or very similar in cone-beam geometry) measured intensity. Geometric alignment can be found post-acquisition by varying the alignment parameter values (with corresponding transformation of the radiographs) until the difference between these pairs of PI-line measurements is minimised. This is a very fast method since it does not require the computationally complex projection or back-projection operations.

For the circular trajectory only a subset of the parameters can be determined since the PI-lines all lie on the central row of the radiograph. The helical trajectory is better suited since the PI-lines are more distributed over the entire detector area [see Fig. 12(a)] and Kingston *et al.* [41] showed that PI-line alignment is more robust than tomogram sharpness but less precise. The distribution of PI-lines over the detector for the SFT is ideal for alignment as it uniformly samples the detector [see Fig. 12(b)] giving improved sensitivity to detector rotation misalignments. The set of PI-lines in Fig. 12 was binned by eight, i.e., used $M = 600/8 = 75$. Therefore, $N = 68$ voxels and $E = 96$. The HT has $\Omega = 375$, and the SFT has $\Omega = 286$.
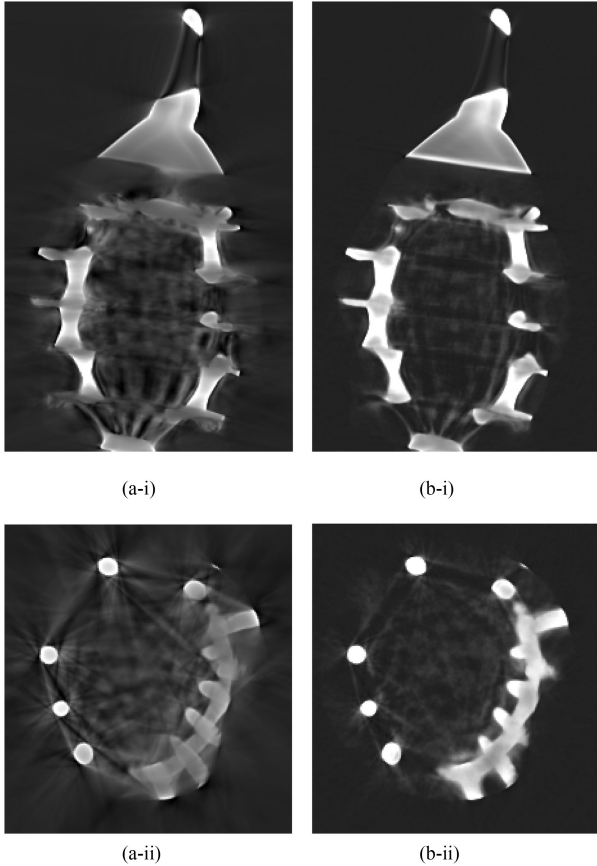
(a-i)　　　　　　　　(b-i)

(a-ii)　　　　　　　　(b-ii)

Fig. 13.　Registered 2D (i) horizontal and (ii) vertical slices through a 25.4 mm diameter pendant made of timber injected with pewter using (a) double-helical trajectory (maximum pitch used according to (5) as $P = 51.49$ mm, $Q = 1440$ per helix, $\Omega = 2294$ per helix) with each helix reconstructed by KFBP and averaged, (b) space-filling trajectory (with $Z = HR/L = 51.51$, $E = 1440$, $\Omega = 1902$) reconstructed using multi-grid BPF method described in [35]. The total scan time for each experiment is similar. Greyscale window: [black = 0.183 mm^{-1}, white = 0.732 mm^{-1}].

Another indication that the SFT is insensitive to perturbations is that the SFT is well-behaved under motion of the specimen/components during scanning. For the SFT, the source rotates relatively rapidly about the specimen with time and with z-translation; any motion that is smooth in time or with stage translation causes a blurry but geometrically faithful reconstruction. Consequently, re-projecting this degraded tomogram (to simulate the experiment) yields a blurry but aligned set of radiographs to which the measured data can be registered. Using the iterative reprojection method set out by Dengler [21] for aligning electron tomography data, Latham *et al.* showed convergence given SFT data is an order of magnitude faster than that given the equivalent HT data [42]. Latham *et al.* showed, that this reprojection method can be integrated into the multi-grid IR scheme developed for the SFT [35] for very little computational cost (2D registration per radiograph) and converges in the first multi-scale iteration.

B. Sensitivity to Beam-hardening/Metal Artifacts

The SFT is also less sensitive to perturbations of data values resulting from e.g., the non-linear remapping of data due to

X-ray beam-hardening or metal inclusions. The isotropic nature of the SFT causes the streak artifacts from such perturbations to be distributed over the largest possible solid-angle; this minimises impact on image quality. An extreme example demonstrating the improved fidelity from real data is presented in Fig. 13. Here a pendant made of timber and pewter was imaged with both double-helix and space-filling trajectories. Tomographic results will depend on the reconstruction algorithm used; although different algorithms were used for each trajectory, neither used any beam-hardening models or spectral information. The sample was placed $R = 39.98$ mm from the micro-focus X-ray source. A 400 mm $\times$ 400 mm detector with a pixel size of 0.278 mm (i.e., 1520 $\times$ 1520 pixel array) was situated $L = 336.3$ mm from the source. The accelerating voltage of the X-ray source was 120 kV and heavy filtering was applied to the X-rays (1.2 mm stainless-steel) resulting in a high energy spectrum, making the timber almost invisible in the tomogram. Although artifacts are still visible in the results using the SFT, and segmentation would still be non-trivial, a significant improvement in image quality can be observed. This is primarily due to the properties of the trajectory and not the difference in reconstruction algorithms used.

VIII. CONCLUSION

Traditional X-ray source trajectories are continuous due to either: a) practical reasons such as very rapid (or even non-stop) rotation and short acquisition times for the case of medical and synchrotron CT, or b) to enable differentiation as part of analytical reconstruction. Micro-CT is not restricted by (a) due to inherently low-flux and relatively long radiograph acquisition times, and the development of general purpose GPUs, that are particularly suited to projection/back-projection calculations, has made IR schemes the natural choice even for 3D tomography with large datasets [43]. Given these considerations, we have introduced a family of sparse discrete scanning trajectories. These trajectories sample the space of possible viewing angles in a more uniform manner compared with traditional line-trajectories. These *space-filling trajectories* are maximally isotropic for typical system geometries, giving more uniform resolution and signal-to-noise ratio than the helical trajectory. The isotropic nature provides an approximately shift-invariant point-spread-function under back-projection; the straight-forward filtering of this inverse filter (as developed by Colsher for PET [33]) produces an effective pre-conditioner to speed convergence of iterative reconstruction. The SFT provides maximally independent information that has a better condition number yielding improved data acquisition efficiency. The SFT has a lower sensitivity to perturbations than the helical trajectory. We have shown that it is well behaved under specimen and component misalignment or motion; the effects of which are readily detected, quantified and corrected. Streak artifacts from beam-hardening and metal inclusions are also reduced compared with the HT, even without any attempt at correction. The SFT along with the multigrid reconstruction scheme outlined in [35] lays a foundation for more general application of iterative reconstruction techniques in high resolution X-ray CT to improve acquisition efficiency and image quality.

ACKNOWLEDGMENT

REFERENCES

[1] M. Paziresh, A. Kingston, S. Latham, W. Fullagar, and G. Myers, "Tomography of atomic number and density of materials using dual-energy imaging and the Alvarez and Macovski attenuation model," *J. Appl. Phys.*, vol. 119, no. 21, 2016, Art. no. 214901.

[2] V. Cnudde and M. N. Boone, "High-resolution x-ray computed tomography in geosciences: A review of the current technology and applications," *Earth-Sci. Rev.*, vol. 123, pp. 1–17, 2013.

[3] S. Schlüter, A. Sheppard, K. Brown, and D. Wildenschild, "Image processing of multiphase images obtained via x-ray microtomography: A review," *Water Resour. Res.*, vol. 50, no. 4, pp. 3615–3639, 2014.

[4] P. J. Withers and M. Preuss, "Fatigue and damage in structural materials studied by x-ray tomography," *Annu. Rev. Mater. Res.*, vol. 42, pp. 81–103, 2012.

[5] L. Feldkamp, L. Davis, and J. Kress, "Practical cone-beam algorithm," *J. Opt. Soc. Amer. A*, vol. 1, no. 6, pp. 612–619, 1984.

[6] H. Tuy, "An inverse formula for cone-beam reconstruction," *SIAM J. Appl. Math.*, vol. 43, pp. 546–552, 1983.

[7] A. Katsevich, "Theoretically exact filtered backprojection-type inversion algorithm for spiral CT," *SIAM J. Appl. Math.*, vol. 62, no. 6, pp. 2012–2026, 2002.

[8] T. Varslot, A. Kingston, A. Sheppard, and A. Sakellariou, "Fast high-resolution micro-CT with exact reconstruction methods," *Proc. SPIE Develop. X-Ray Tomography VII*, vol. 7804, 2010, Art. no. 780413.

[9] A. Sheppard *et al.*, "Techniques in helical scanning, dynamic imaging, and image segmentation for improved quantitative analysis with x-ray micro-CT," *Nucl. Instrum. Methods Phys. Res., Sect. B*, vol. 324, pp. 49–56, 2014.

[10] T. Varslot, A. Kingston, G. Myers, and A. Sheppard, "Considerations for high-magnification high-cone-angle helical micro-CT," *Proc. SPIE Develop. X-Ray Tomography VIII*, vol. 8506, 2012, Art. no. 850614.

[11] A. Katsevich, "3PI algorithms for helical computer tomography," *Adv. Appl. Math.*, vol. 36, no. 3, pp. 213–250, 2006.

[12] Y. Zou and X. Pan, "Image reconstruction on PI-lines by use of filtered backprojection in helical cone-beam CT," *Phys. Med. Biol.*, vol. 49, no. 12, pp. 2717–2731, 2004.

[13] K. Tam, S. Samarasekera, and F. Sauer, "Exact cone beam CT with a spiral scan," *Phys. Med. Biol.*, vol. 43, no. 4, pp. 1015–1024, 1998.

[14] P. Danielsson, P. Edholm, J. Eriksson, and M. Magnusson, "Towards exact reconstruction for helical cone-beam scanning of long objects. A new detector arrangement and a new completeness condition," in *Proc. Int. Meeting Fully 3D Image Reconstruction Radiol. Nucl. Med.*, 1997, pp. 141–144.

[15] C. Bontus, R. Proksa, J. Timmer, T. Köhler, and M. Grass, "Movement artifacts in helical ct cone-beam reconstruction," in *Proc. Int. Meeting Fully 3D Image Reconstruction Radiol.Nucl. Med.*, 2001, pp. 199–202.

[16] H. Yu and G. Wang, "Studies of artifacts of the katsevich algorithm for spiral cone-beam ct," *Proc. SPIE Develop. X-Ray Tomography IV*, vol. 5535, pp. 540–549, 2004.

[17] T. Köhler, R. Proksa, C. Bontus, and M. Grass, "Artifact analysis of approximate cone-beam CT algorithms," *Med. Phys.*, vol. 29, pp. 51–64, 2002.

[18] T. Varslot, A. Kingston, G. Myers, and A. Sheppard, "High-resolution helical cone-beam micro-CT with theoretically-exact reconstruction from experimental data," *Med. Phys.*, vol. 38, no. 10, pp. 5459–5476, 2011.

[19] B. De Man, J. Nuyts, P. Dupont, G. Marchal, and P. Suetens, "An iterative maximum-likelihood polychromatic algorithm for CT," *IEEE Trans. Med. Imag.*, vol. 20, no. 10, pp. 999–1008, Oct. 2001.

[20] A. Kingston, A. Sakellariou, T. Varslot, G. Myers, and A. Sheppard, "Reliable automatic alignment of tomographic projection data by passive auto-focus," *Med. Phys.*, vol. 38, no. 9, pp. 4934–4945, 2011.

[21] J. Dengler, "A multi-resolution approach to the 3d reconstruction from an electron microscope tilt series solving the alignment problem without gold particles," *Ultramicroscopy*, vol. 30, no. 3, pp. 337–348, 1989.

[22] J. Nuyts, B. De Man, J. A. Fessler, W. Zbijewski, and F. J. Beekman, "Modelling the physics in the iterative reconstruction for transmission computed tomography," *Phys. Med. Biol.*, vol. 58, no. 12, pp. R63–R96, 2013.

[23] G. Myers, A. Kingston, T. Varslot, M. Turner, and A. Sheppard, "Dynamic tomography with a priori information," *Appl. Opt.*, vol. 50, no. 20, pp. 3685–3690, 2011.

[24] A. J. Rockmore and A. Macovski, "A maximum likelihood approach to emission image reconstruction from projections," *IEEE Trans. Nucl. Sci.*, vol. 23, no. 4, pp. 1428–1432, Aug. 1976.

[25] P. Gilbert, "Iterative methods for the three-dimensional reconstruction of an object from projections," *J. Theor. Biol.*, vol. 36, no. 1, pp. 105–117, 1972.

[26] Z. Yu, J.-B. Thibault, C. A. Bouman, K. D. Sauer, and J. Hsieh, "Fast model-based x-ray CT reconstruction using spatially nonhomogeneous ICD optimization," *IEEE Trans. Image Process.*, vol. 20, no. 1, pp. 161–175, Jan. 2011.

[27] F. Noo, R. Clack, and M. Defrise, "Cone-beam reconstruction from general discrete vertex sets using radon rebinning algorithms," *IEEE Trans. Nucl. Sci.*, vol. 44, no. 3, pp. 1309–1316, Jun. 1997.

[28] R. A. Crowther, D. J. DeRosier, and A. Klug, "The reconstruction of a three-dimensional structure from projections and its application to electron microscopy," *Proc. Roy. Soc. London A*, vol. 317, no. 1530, pp. 319–340, Jun. 1970.

[29] W. Thompson and W. Lionheart, "Optimisation of the source firing pattern for real time cone-beam tomography," in *Proc. 11th Int. Meeting Fully 3D Image Reconstruction Radiol. Nucl. Med.*, 2011, pp. 335–338.

[30] A. Kingston, G. Myers, S. Latham, H. Li, and A. Sheppard, "Optimized x-ray source scanning trajectories for iterative reconstruction in high cone-angle tomography," *Proc. SPIE Develop. X-ray Tomography X*, vol. 9967, 2016, Art. no. 9967.12.

[31] C. Bontus, R. Proksa, and T. Kohler, "New saddle trajectories for CT," in *Proc. IEEE Nucl. Sci. Symp. Conf. Record*, 2006, vol. 4, pp. 2309–2310.

[32] W. Fullagar, M. Paziresh, S. Latham, G. Myers, and A. Kingston, "The index of dispersion as a metric of quanta – Unravelling the fano factor," *Acta Crystallogr. Struct. Sci. Cryst. Eng. Mater. B*, vol. 73, pp. 675–695, 2017.

[33] J. Colsher, "Fully-three-dimensional positron emission tomography," *Phys. Med. Biol.*, vol. 25, no. 1, pp. 103–115, 1980.

[34] R. Proksa, T. Kohler, M. Grass, and J. Timmer, "The n-PI-method for helical cone-beam CT," *IEEE Trans. Med. Imag.*, vol. 19, no. 9, pp. 848–863, Sep. 2000.

[35] G. Myers *et al.*, "Rapidly converging multigrid reconstruction of cone-beam tomographic data," *Proc. SPIE Develop. X-Ray Tomography X*, vol. 9967, 2016, Art. no. 99671M.

[36] J. W. Stayman and J. H. Siewerdsen, "Task-based trajectories in iteratively reconstructed interventional cone-beam CT," in *Proc. Int. Meeting Fully 3D Image Reconstruction Radiol.Nucl. Med.*, 2013, pp. 257–260.

[37] F. Natterer, *The Mathematics of Computerized Tomography*, vol. 32. Philadelphia, PA, USA: SIAM, 1986.

[38] W. Thompson, "Source firing patterns and reconstruction algorithms for a switched source, offset detector CT machine," Ph.D. dissertation, , Faculty Eng. Phys. Sci., Manchester Inst. Math. Sci., School Math., The Univ. Manchester, Manchester, U.K., 2010.

[39] W. Thompson, W. Lionheart, and D. Oberg, "Reduction of periodic artefacts for a switched-source x-ray CT machine by optimising the source firing pattern," in *Proc. 12th Int. Meeting Fully 3D Image Reconstruction Radiol. Nucl. Med.*, 2013, pp. 345–348.

[40] L. Landweber, "An iteration formula for fredholm integral equations of the RST kind," *Amer. J. Math.*, vol. 73, pp. 615–624, 1951.

[41] A. Kingston *et al.*, "Geometric alignment of helical tomographic projection data using PI-lines," in *Proc. 1st Int. Conf. Tomography Mater. Struct.*, 2013, pp. 101–104.

[42] S. Latham, A. Kingston, B. Recur, G. Myers, and A. Sheppard, "Multi-resolution radiograph alignment for motion correction in x-ray micro-tomography," *Proc. SPIE Develop. X-ray Tomography X*, vol. 9967, 2016, Art. no. 9967.10.

[43] G. Myers *et al.*, "High cone-angle x-ray computed micro-tomography with 186 gigavoxel datasets,"*Proc. SPIE Develop. X-ray Tomography X*, vol. 9967, 2010, Art. no. 99670U.

Authors' photographs and biographies not available at the time of publication.